RESEARCH ARTICLE

Convergence in non-associated plasticity and fracture propagation for standard, rate-dependent, and Cosserat continua

Tim Hageman | Sepideh Alizadeh Sabet | René de Borst

Department of Civil and Structural Engineering, University of Sheffield, Sheffield, UK

Correspondence
René de Borst, Department of Civil and Structural Engineering, University of Sheffield, Sheffield S1 3JD, UK.
Email: r.deborst@sheffield.ac.uk

Funding information
H2020 European Research Council, Grant/Award Number: 664734

Abstract

The use of pressure-dependent plasticity models with a non-associated flow rule causes a loss of the well-posedness for sufficiently low hardening rates. Apart from a mesh dependence, this can result in poor convergence, or even divergence of the iterative procedure employed to find an equilibrium configuration. This can be aggravated when other nonlinear, dissipative mechanisms are introduced, for instance the propagation of cracks. This is demonstrated rigorously, as well as the regularizing effect of adding viscosity or employing a Cosserat continuum. In both cases the regularization is independent of the value of the internal length scale for a fairly wide range of parameters. The spatial discretization has been done using T-splines, and the fracture is modeled using interface elements and propagated using mesh line insertions. The time integration has been done by an implicit Newmark scheme. The use of proper regularization techniques makes an implicit scheme feasible, resulting in a reduction in the number of time steps by an order of magnitude.

KEYWORDS

Cosserat continuum, fracture, non-associated plasticity, T-splines, viscoplasticity

1 | INTRODUCTION

Non-associated plasticity is a common framework for modeling inelasticity in geomaterials, such as soils, concrete, and rocks.[1] Different from most plasticity formats used to model the inelastic straining in metals, the flow rule is not defined by the gradient of the yield function. Rather, a separate plastic potential is postulated and the plastic strain rate tensor is derived by differentiating the plastic potential with respect to the stress tensor. The underlying physical reason is that the plastic volume change which is predicted by an associated flow rule, that is, when the plastic strain rates are derived from the yield function, vastly overpredicts the measured plastic volume changes. Especially in kinematically constrained situations this can lead to very different values of the normal stresses, and because of this, plastic yielding can be affected significantly.

A consequence of using a non-associated flow rule is that the tangent operator used in Newton-Raphson procedures to arrive at a global equilibrium state in nonlinear systems becomes non-symmetric.[2] While this nonsymmetry has regularly been assumed to be the reason for slow convergence, or even failure to converge,[3,4] it has recently been argued that the

convergence difficulties of plasticity models with a non-associated flow rule are actually rooted in the loss of ellipticity which occurs at sufficiently low rates of hardening, including ideal plasticity.[5] The local loss of ellipticity of plasticity models with a non-associated flow rule, and the ensuing loss of well-posedness of associated boundary value problems has been known for long,[6] but has not been linked to issues like a severe mesh dependence and failure to reach an equilibrium state until recently.[5,7] While convergence difficulties can be observed clearly when using Newton-Raphson solvers, where divergence is actually often seen, it also affects Picard-type solvers as the latter exhibit a lower rate of convergence than is typically observed for well-posed initial/boundary value problems.

The convergence difficulties encountered in solving plasticity models with a non-associated flow rule are aggravated when simultaneously considering other dissipative mechanisms. An example of geomechanical and geophysical interest is the propagation of a shear fault, where off-fault plasticity is typically described using a Drucker-Prager or Mohr-Coulomb yield criterion with a non-associated flow rule. Previous simulations, using finite element[8,9] or finite difference methods,[10] have demonstrated the effect of including the plastic material behavior on the propagation velocity of the fault,[8] and on the stresses required to initialize and maintain fracture propagation.[11] While these simulations have shown the importance of including plasticity, fine meshes were needed to obtain accurate results. Furthermore, due to the use of explicit time-discretized methods, small time steps were required to obtain stable simulations. Even then, the explicit character of the simulations does not guarantee that the solutions indeed satisfy the balance of momentum.

As noted above, loss of well-posedness of the initial/boundary value problem also causes a severe discretization dependence.[12] One method to restore well-posedness, and thus to avoid an excessive mesh dependence, is the use of a Cosserat continuum.[13] Through the addition of rotational degrees of freedom, micro-curvatures are introduced in the kinematics, which are related to microstructural couple-stresses via a bending modulus like material parameter.[14] Since the quotient of a bending modulus and the Young's modulus has the dimension of length, an internal length scale is thus effectively introduced in this enhanced continuum model, causing localization zones to have a finite width and therefore removing an excessive mesh dependence. Cosserat continua are often used in geomechanics, for instance to model localized shear bands,[15-17] to analyze failures due to deep excavations,[18] and to simulate rock joints.[19,20]

While the Cosserat continuum has been used successfully to regularize problems that involve decohesion,[12,21,22] it has been shown more recently that it is also effective as a localization limiter for problems which involve non-associated plasticity.[5,7] As suggested above, another advantage of restoring well-posedness by using a Cosserat continuum is the improvement in convergence characteristics of the iterative procedure which aims at satisfying the momentum balance of the spatially discretized system.[23]

Another regularization method is the inclusion of viscosity in the plasticity model.[24] A time scale, and hence a length scale is introduced into the initial value problem,[25-28] allowing plasticity to spread over a zone of finite dimensions. However, under quasi-static loading conditions, the inclusion of viscosity only weakly regularizes the problem and an ill-posed problem is retrieved in the rate-independent limit.[29] In fully dynamic computations, the inclusion of viscosity has also been shown to increase the stability and the maximum time step when an explicit time discretization scheme is used.[30] In implicit schemes, using viscoplasticity prevents spurious oscillations for low-order elements.[31]

As noted above, simulations of fault propagation with off-fault plasticity normally require extremely fine discretizations. Herein, we use spline-based discretization methods to allow coarser meshes compared to standard finite elements.[32,33] The use of splines also allows higher-order continuity to be achieved across element boundaries, resulting in continuous, or even smooth stress fields. T-splines allow for local refinement to increase the accuracy where needed,[34-36] and the propagation of discontinuities.[37] Elasto-plastic simulations have shown the advantages of using this discretization technology, resulting in an improved accuracy without being hindered by issues such as mesh locking.[38] The higher-order continuity has also been shown to be beneficial in the simulation of more complex problems, like gradient-dependent plasticity,[39] or three-dimensional domains.[40]

Our aim is to simulate fracture propagation in the presence of non-associated, off-fracture plasticity using an implicit time-discretized method to analyze the efficacy of a Cosserat continuum and viscoplasticity to properly regularize the boundary value problem for a range of values of the internal length scale, from smaller than the element size to the same order of magnitude as the dimensions of the problem. In the presence of a propagating fracture, it is not possible to ensure smooth stress changes. For this reason we have carefully analyzed the stabilizing effects of either using a Cosserat continuum or using visco-plasticity when a sudden change in stress occurs due to stepwise crack propagation as a consequence of finite time steps. Finally, we will analyze how the fracture propagation and plastic strains depend on the size of the elements at the interface.

2 | GOVERNING EQUATIONS

We will model fracture propagation first using a standard continuum and subsequently using a Cosserat continuum under plane-strain conditions. While the equations detailed below are for a Cosserat continuum, they are presented in such a manner that they can also directly be related to the governing equations for a standard continuum.

2.1 | Continuum plasticity

The momentum balance for a continuum is given by:

$$\rho \ddot{\boldsymbol{u}} - \boldsymbol{L}^T \boldsymbol{\sigma} = 0, \tag{1}$$

where for a Cosserat continuum, the vector $\boldsymbol{u} = [u_x, u_y, \omega_z]^T$ includes the linear displacements u_x, u_y, and the Cosserat micro-rotational degree of freedom ω_z. With the stress vector $\boldsymbol{\sigma}^T = [\sigma_{xx}, \sigma_{yy}, \sigma_{zz}, \sigma_{xy}, \sigma_{yx}, m_{xz}/\ell_c, m_{yz}/\ell_c]$ with σ_{xx} etc. the Cauchy stress tensor components, m_{xz}, m_{yz} the couple-stress tensor components, and ℓ_c the Cosserat internal length scale, we have:

$$\rho = \begin{bmatrix} \rho & 0 & 0 \\ 0 & \rho & 0 \\ 0 & 0 & \Theta \end{bmatrix} \quad \boldsymbol{L}^T = \begin{bmatrix} \frac{\partial}{\partial x} & 0 & 0 & 0 & \frac{\partial}{\partial y} & 0 & 0 \\ 0 & \frac{\partial}{\partial y} & 0 & \frac{\partial}{\partial x} & 0 & 0 & 0 \\ 0 & 0 & 0 & -1 & 1 & \ell_c \frac{\partial}{\partial x} & \ell_c \frac{\partial}{\partial y} \end{bmatrix}, \tag{2}$$

where ρ is the density and $\Theta = 2\rho\ell_c^2/(1 + \nu)$ the rotational inertia.[21]

As usual the stress rate is linearly related to the strain rate by:

$$\dot{\boldsymbol{\sigma}} = \boldsymbol{D}^e(\dot{\boldsymbol{\varepsilon}} - \dot{\boldsymbol{\varepsilon}}^p), \tag{3}$$

with $\boldsymbol{D}^e$ the linear-elastic stiffness matrix for a Cosserat continuum. The total strain vector $\boldsymbol{\varepsilon}$ is defined as $\boldsymbol{\varepsilon} = [\varepsilon_{xx}, \varepsilon_{yy}, \varepsilon_{zz}, \varepsilon_{xy}, \varepsilon_{yx}, \ell_c\kappa_{xz}, \ell_c\kappa_{yz}]$, with the total strain related to the displacements by:

$$\boldsymbol{\varepsilon} = \boldsymbol{L}\boldsymbol{u}. \tag{4}$$

To keep matters as simple as possible we will use Drucker-Prager plasticity with a non-associated flow rule, defined by the yield function:

$$f = \sqrt{3J_2} + \alpha p - k, \tag{5}$$

and the plastic potential function:

$$g = \sqrt{3J_2} + \beta p, \tag{6}$$

with J_2 the second invariant of the deviatoric stresses and p the pressure (positive for tension). For the Cosserat continuum the extended definition for J_2 has been used:[13,21,41]

$$J_2 = \frac{1}{2}\boldsymbol{\sigma}^T \boldsymbol{P} \boldsymbol{\sigma} = \frac{1}{2} \begin{bmatrix} \sigma_{xx} \\ \sigma_{yy} \\ \sigma_{zz} \\ \sigma_{xy} \\ \sigma_{yx} \\ m_{xz}/\ell_c \\ m_{yz}/\ell_c \end{bmatrix}^T \begin{bmatrix} 2/3 & -1/3 & -1/3 & 0 & 0 & 0 & 0 \\ -1/3 & 2/3 & -1/3 & 0 & 0 & 0 & 0 \\ -1/3 & -1/3 & 2/3 & 0 & 0 & 0 & 0 \\ 0 & 0 & 0 & 1/2 & 1/2 & 0 & 0 \\ 0 & 0 & 0 & 1/2 & 1/2 & 0 & 0 \\ 0 & 0 & 0 & 0 & 0 & 1 & 0 \\ 0 & 0 & 0 & 0 & 0 & 0 & 1 \end{bmatrix} \begin{bmatrix} \sigma_{xx} \\ \sigma_{yy} \\ \sigma_{zz} \\ \sigma_{xy} \\ \sigma_{yx} \\ m_{xz}/\ell_c \\ m_{yz}/\ell_c \end{bmatrix}. \tag{7}$$

The constants α, β, and k are related to the angle of internal friction ϕ, the dilatancy angle ψ, and the cohesion c by:

$$\alpha = \frac{6 \sin \phi}{3 - \sin \phi} \quad \beta = \frac{6 \sin \psi}{3 - \sin \psi} \quad k = c \frac{6 \cos \phi}{3 - \sin \phi}.$$

For the cases in which viscoplasticity is included as a regularization mechanism, a linear version of the Perzyna model is used, so that:[2]

$$\dot{\varepsilon}^p = \frac{f}{\eta \sigma_0} \boldsymbol{m} \quad \text{if} \quad f > 0, \tag{8}$$

with η the viscosity parameter, σ_0 the reference stress, and $\boldsymbol{m}$ the direction of plastic flow, given by:

$$\boldsymbol{m} = \frac{\boldsymbol{m}^*}{\|\boldsymbol{m}^*\|} \quad \boldsymbol{m}^* = \begin{cases} \frac{\partial g}{\partial \sigma} & \text{if } p \le k \\ (\boldsymbol{D}^e)^{-1}(\boldsymbol{\sigma}^{\text{trial}} - \boldsymbol{\sigma}^{\text{apex}}) & \text{if } p > k \end{cases}, \tag{9}$$

using the trial stress $\boldsymbol{\sigma}^{\text{trial}}$ and the stress at the apex of the Drucker-Prager cone $\boldsymbol{\sigma}^{\text{apex}}$.

The viscosity parameter sets the time scale over which the plastic strain spreads. The use of viscoplasticity introduces a length scale, which can be approximated as:[25,28]

$$\ell_v = \frac{2 \eta \sigma_0}{\sqrt{\rho E}}. \tag{10}$$

The width of the localization zone is of the same order as this length scale, and is weakly dependent on how the loading is applied.[25]

When no viscosity is included, the yield function is bounded by $f \le 0$ and the plastic flow is determined from:

$$\hat{\varepsilon}^p = \hat{\lambda} \boldsymbol{m}, \tag{11}$$

with $\hat{\square}$ indicating the path-dependent derivative of the variable, in contrast to the time-dependent derivatives indicated by $\dot{\square}$ in, for instance, the acceleration in Equation (1). This distinction is made to differentiate between the physical concept of time and an abstract concept used, for instance, in inviscid plasticity, where "time" is merely used to order the sequence of events.

2.2 | Discrete fracture

The fracture is modeled using a slip model, which relates the tangential component of the traction τ_t on the faces of the fracture to the slip to differences in tangential displacements, $[\![dx]\!]$ and the normal stress τ_n which compresses the fracture:

$$\tau_t = f_r \tau_n + (f_p - f_r) \, \tau_n \exp(-2 [\![dx]\!] / D_c), \tag{12}$$

with f_r and f_p the residual and peak coefficients of friction. The maximum difference in tangential displacement $[\![dx]\!]$ is treated as a history variable, indicating the maximum tangential displacement difference between the top and bottom walls that has occurred. Therefore, $[\![dx]\!]$ is equal to the tangential displacement $[\![u_t]\!]$, or constant if the tangential displacement is lower than the maximum tangential displacement that has occurred previously. Finally, D_c is the weakening distance, given by $D_c = 2\mathcal{G}_c/(f_p \tau_n - f_r \tau_n)$ with $\mathcal{G}_c$ the fracture energy. This exponential degradation function, shown in Figure 1, was preferred to the more commonly used linear degradation model[8,42] to retain a smooth function which does not artificially disturb the convergence of the nonlinear iterative solver.

To prevent negative fracture opening heights, a dummy stiffness d_n has been used:

$$\tau_n = \begin{cases} d_n [\![u_n]\!] & \text{if} \quad [\![u_n]\!] < 0 \\ 0 & \text{if} \quad [\![u_n]\!] \ge 0 \end{cases}, \tag{13}$$
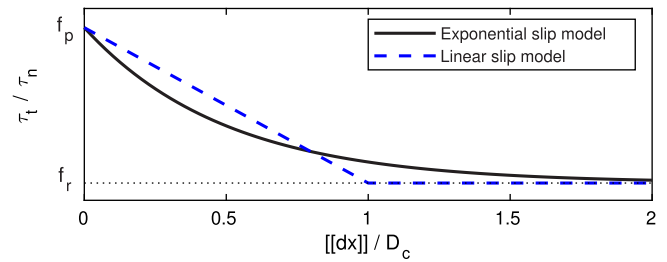
with $[\![u_n]\!]$ the jump in the normal displacement at the interface. This allows the normal component of the traction to be linearly related to the opening height, facilitating the evaluation of Equation (12). Finally, the Cosserat microrotation is assumed to be continuous in the case of compressed fractures. This is enforced by using a dummy stiffness d_ω for the couple-traction at the interface:

$$\tau_\omega / \ell_c^2 = d_\omega [\![\omega]\!]. \tag{14}$$

It is noted that due to the inclusion of the discrete slip model, two dissipative mechanisms are present which can be related to inelastic effects. The slip model can represent the small-scale yielding which is localized in an area near the fracture, whereas the Drucker-Prager plasticity models the off-fracture large-scale plasticity in the interior of the domain.

3 | DISCRETIZATION AND INTEGRATION

3.1 | Spatial discretization

The spatial discretization has been done using T-splines.[32,43] This allows accurate displacement and stress fields to be obtained with a reduced number of degrees of freedom compared to the use of Lagrangian interpolants,[44] and allows refinement near the fracture in contrast to B-splines. Another advantage of using T-splines is the ability to insert interface elements only for the fractured elements. The T-splines are used in a similar manner as Lagrangian finite elements by using Bézier extraction, allowing the internal force vector to be constructed in an element-wise manner.[34,45] While the displacement and Cosserat rotation can use unequal order interpolation polynomials, it was chosen to use cubic T-splines for both of these variables. The use of cubic T-splines results in a C^2 inter-element continuity for the displacements and rotations, and hence in continuous and smooth stress fields. The spatial integration is performed using a standard Gauss integration scheme.

The fracture is modeled using interface elements and it is propagated using mesh line insertions.[35,37] By inserting mesh lines in the parametric domain at the same location as pre-existing mesh lines, the inter-element continuity can be reduced locally. If the fracture had been propagated by locally reducing from a C^2 to a C^{-1} continuity, the control points of the mesh would have changed location, necessitating a remap not only of the displacements, but also a recalculation of the history variables at the new control points.[46] To prevent this, and to eliminate a source of potential errors, we have pre-inserted a C^0 continuity along a predetermined fracture path. Mesh line insertion to reduce the continuity from C^0 to C^{-1} results in only a duplication of the control point at the interface, without altering the location of this or any other control point. Therefore, the state and history variables associated with the duplicated control points can easily be moved to the new control points.

The fracture is propagated if for all integration points in the element ahead of the fracture the shear stress σ_{yx} exceeds the mode-II fracture strength. This fracture strength depends on the normal stresses through $f_t = f_p \sigma_{yy}$, assuming a horizontal fracture.[8]

3.2 | Boundary conditions

On the boundaries of the domain, absorbing boundary conditions are imposed to prevent reflecting stress waves. Assuming the effects of the Cosserat rotation are small on the overall wave propagation near the edges of the domain, these

absorbing boundaries are defined in a local coordinate system by:

$$\boldsymbol{\tau} = \boldsymbol{C}\dot{\boldsymbol{u}}, \tag{15}$$

with the damping matrix, which depends on the pressure and shear wave speeds c_p and c_s, as follows:[47-49]

$$\boldsymbol{C} = \rho \begin{bmatrix} c_p & 0 & 0 \\ 0 & c_s & 0 \\ 0 & 0 & 0 \end{bmatrix}$$

3.3 | Integration of the stress rate-strain rate relation

At integration point level, the stresses are predicted assuming elastic deformations in the current time increment:

$$\boldsymbol{\sigma}^{trial} = \boldsymbol{D}^e(\boldsymbol{B}\boldsymbol{u}_{t+\Delta t} - \boldsymbol{\varepsilon}_t^P), \tag{16}$$

with $\boldsymbol{B} = \boldsymbol{L}\boldsymbol{N}$ and $\boldsymbol{N}$ contains the cubic interpolants of the element at the integration point. The trial stress is subsequently substituted in the yield function, Equation (5), to determine whether plastic deformations occur or not. In the case of plastic deformations, the following two discrete conditions must be fulfilled:

$$0 = \boldsymbol{\sigma} - (\boldsymbol{\sigma}^{trial} - \widehat{\Delta\lambda}\boldsymbol{D}^e\boldsymbol{m}), \tag{17a}$$

$$0 = f - \frac{\eta\sigma_0}{\Delta t}\widehat{\Delta\lambda}, \tag{17b}$$

while the case without viscosity is retrieved by setting $\eta = 0$. $\widehat{\Delta\lambda}$ is related to the plastic strain increment through $\widehat{\Delta\varepsilon}_p = \widehat{\Delta\lambda}\boldsymbol{m}$.

Equations (17) are solved in a local iteration loop:

$$\begin{bmatrix} \boldsymbol{\sigma} \\ \widehat{\Delta\lambda} \end{bmatrix}_{j+1} = \begin{bmatrix} \boldsymbol{\sigma} \\ \widehat{\Delta\lambda} \end{bmatrix}_j - \boldsymbol{C}_{eff}^{-1} \begin{bmatrix} \boldsymbol{\sigma} - (\boldsymbol{\sigma}^{trial} - \widehat{\Delta\lambda}\boldsymbol{D}^e\boldsymbol{m}) \\ f - \frac{\eta\sigma_0}{\Delta t}\widehat{\Delta\lambda} \end{bmatrix}_j, \tag{18}$$

with the effective compliance given by:

$$\boldsymbol{C}_{eff} = \begin{bmatrix} \boldsymbol{I} + \widehat{\Delta\lambda}_j\boldsymbol{D}^e\frac{\partial\boldsymbol{m}}{\partial\sigma_j} & \boldsymbol{D}^e\boldsymbol{m} \\ \left(\frac{\partial f}{\partial\sigma_j}\right)^T & -\frac{\eta\sigma_0}{\Delta t} \end{bmatrix}, \tag{19}$$

which is also used to obtain the consistent stiffness matrix $\boldsymbol{D}_{eff}$ when plasticity occurs by selecting the 7×7 submatrix after inverting, starting from the top left corner of the matrix, and multiplying with $\boldsymbol{D}^e\left(\boldsymbol{I} - \widehat{\Delta\lambda}\boldsymbol{D}^e\frac{\partial\boldsymbol{m}}{\partial\sigma^{trial}}\right)$. In the absence of plasticity the effective stiffness equals the elastic stiffness, and if the pressure exceeds that at the apex of the Drucker-Prager yield cone, the material stiffness matrix $\boldsymbol{D}_{eff} = \boldsymbol{0}$ is used in the absence of viscosity.[2]

3.4 | Time discretization

The temporal discretization is done using a Newmark scheme, allowing the velocity and acceleration related to the control points at the new time to be described in terms of the old velocity and acceleration, and the new displacements:

$$\dot{\boldsymbol{u}}_{t+\Delta t} = \frac{\gamma}{\beta\Delta t}(\boldsymbol{u}_{t+\Delta t} - \boldsymbol{u}_t) - \left(\frac{\gamma}{\beta} - 1\right)\dot{\boldsymbol{u}}_t - \left(\frac{\Delta t\gamma}{2\beta} - \Delta t\right)\ddot{\boldsymbol{u}}_t, \tag{20}$$

$$\ddot{\boldsymbol{u}}_{t+\Delta t} = \frac{1}{\beta \Delta t^2}(\boldsymbol{u}_{t+\Delta t} - \boldsymbol{u}_t) - \frac{1}{\beta \Delta t}\dot{\boldsymbol{u}}_t - \left(\frac{1}{2\beta} - 1\right)\ddot{\boldsymbol{u}}_t, \tag{21}$$

with β and γ time integration parameters. This time discretization requires the velocity and acceleration at the old time to be saved in the control points. The resulting discretized equations are given in Appendix A.

Since the resulting discretized equations are dependent on the displacements at the new time, an iterative Newton-Raphson algorithm is used to obtain the new displacements. The convergence at the end of iteration j is evaluated using an energy-based criterion:

$$\text{error}^j = \frac{e^j}{e^1} = \frac{\boldsymbol{f}_{\text{int}}^j \cdot d\boldsymbol{u}^j}{\boldsymbol{f}_{\text{int}}^1 \cdot d\boldsymbol{u}^1}, \tag{22}$$

with $\boldsymbol{f}_{\text{int}}$ the internal force vector obtained using the new displacements, and $d\boldsymbol{u}$ the displacement increment added during the iteration.

The fracture propagation criterion is checked when the converged solution has been reached. Upon propagation of the fracture, and completion of the accompanying mesh line insertion, additional Newton-Raphson iterations are carried out until convergence is reached for the new extension of the discontinuity. This results in a fully implicit time discretization, where both the displacements at $t + \Delta t$ and the fracture length at $t + \Delta t$ are used to update the time step.

3.5 | Implementation aspects

To check whether the fracture should propagate or not, stresses must be known in the extension of the fracture. Interpolation between integration points is inconvenient and not necessarily accurate, thus additional zero-weight integration points are introduced along the element boundaries. These zero-weight integration points are treated in the same manner as the normal integration points, and therefore keep track of the plastic strains at the element boundaries. This allows the stresses required for fracture propagation to be determined in a straightforward manner, and facilitates postprocessing of the plastic strains and the stresses near the discontinuity and the boundaries of the domain. Since T-splines have been used, the displacement gradients can be determined uniquely at the edges of elements, and the stresses are continuous between neighbouring elements.

To maintain quadratic convergence when using the Newton-Raphson method to achieve equilibrium at structural level, the effective stiffness for the first iteration of the next time step was determined from the final state at the end of the previous time step. This generally enhances convergence compared to starting with a fully elastic stiffness matrix, or using the current stress state at the first iteration. It also removes most oscillations due to integration points switching from elastic unloading to plastic loading, and vice versa. This can also be achieved by including a small amount of viscosity, resulting in the return-mapping being performed to states with $f > 0$.

It is finally noted that three different sets of history-dependent variables are used. The first type of history variable is the discontinuity length, and the accompanying discretization using the T-spline mesh. This is only updated if the fracture propagates. The second type is the time-dependent velocity and acceleration at the old time step, $\dot{\boldsymbol{u}}_t$ and $\ddot{\boldsymbol{u}}_t$. These values are updated once the complete time step, including possible fracture propagation, has converged fully. This ensures that updating the velocity and accelerations only influences the results for the next time step. The final set of history variables are the path-dependent variables, here the plastic strains at the old time, ϵ_t^p, and the tangential displacement at the interface, $[\![dx]\!]_t$. These variables depend on the loading path, and therefore on the maximum value attained at convergence in the time step. To properly include the loading and unloading that occurs around the fracture during fracture propagation, these history variables are updated when the discontinuity is propagated and at the end of each time step. This results in the variables ϵ_t^p and $[\![dx]\!]_t$ either coming from the previous time step (at time t), or from the current time step at the instant that the fracture has propagated. It allows the history variable to capture a loading-fracture propagation-unloading behavior within the time step, avoiding spurious plastic strains resulting from too high stresses before fracture propagation.

4 | CASE STUDY: PLASTICITY WITHOUT FRACTURE PROPAGATION

We first show the effects of viscoplasticity and a Cosserat continuum on the convergence in the absence of propagating fractures. The domain consists of a rectangle, 1 m × 2 m, with a central edge fracture of 0.25 m, which cannot propagate,
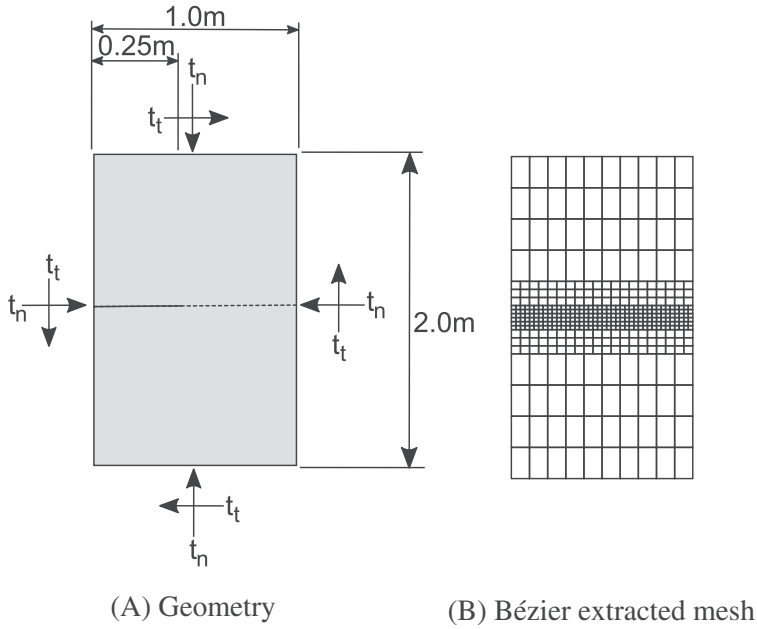
FIGURE 2 Geometry and mesh used for the case without fracture propagation. (A) Geometry; (B) Bézier extracted mesh

(A) Geometry

(B) Bézier extracted mesh
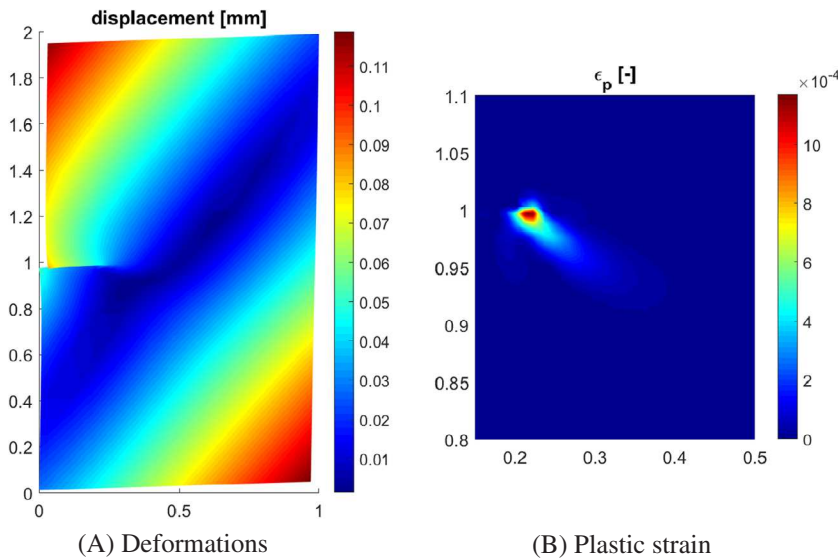
FIGURE 3 Deformations and plastic strain at $t = 1.02$ s for $t_t = 0.4$ MPa [Color figure can be viewed at wileyonlinelibrary.com]

(A) Deformations

(B) Plastic strain

see Figure 2(A). A normal traction $t_n = 1.0$ MPa is applied to the boundaries, and two values for the shear tractions are used, $t_t = 0.2$ MPa with time step size $\Delta t = 0.1$ ms and $t_t = 0.4$ MPa with $\Delta t = 1$ ms. The applied tractions result in plastic strains near the fracture tip. To start from an initial configuration which is in equilibrium no plasticity is allowed for the first 1.0 s of the simulation. Thereafter, plasticity is allowed and a sudden burst of plasticity occurs around the fracture tip, as shown in Figure 3. Due to inertial effects, the plastic strain evolves over several time steps. This case was chosen as being representative of the sudden changes in stress, and the accompanying plastic strain, which happen during fracture propagation in more complex cases.

The material is assumed to be characterized by a value for Young's modulus $E = 10$ GPa, Poisson ratio $\nu = 0.25$, Cosserat shear modulus $G_c = 4$ GPa, and density $\rho = 2500$ kg/m^3. The non-associated Drucker-Prager plasticity model is cohesionless ($c = 0$), has an angle of internal friction $\phi = 30°$, and is nondilatant (dilatancy angle $\psi = 0°$). For the viscosity parameter, several values have been investigated: $\eta\sigma_0 = 0$ Pa · s (no viscoplasticity), $\eta\sigma_0 = 10^3$ Pa · s, $\eta\sigma_0 = 10^4$ Pa · s, $\eta\sigma_0 = 10^5$ Pa · s, and $\eta\sigma_0 = 10^6$ Pa · s. Using Equation (10), these values for the viscosity parameter can be shown to correspond to the length scales $\ell_v = 0.4$, 4, 40 mm (comparable to the element size), and 400 mm (comparable to size of the total domain), respectively. For the Cosserat continuum the following values of the internal length scale have been used: $\ell_c = 0.1$ mm, $\ell_c = 1.0$ mm, $\ell_c = 10$ mm, and $\ell_c = 100$ mm. Since the width of the localization zone in a Cosserat

FIGURE 4 Convergence behavior for a standard continuum with and without visco-plasticity, and using a Cosserat continuum without visco-plasticity for $t_t = 0.2$ MPa, $\Delta t = 0.1$ ms [Color figure can be viewed at wileyonlinelibrary.com]
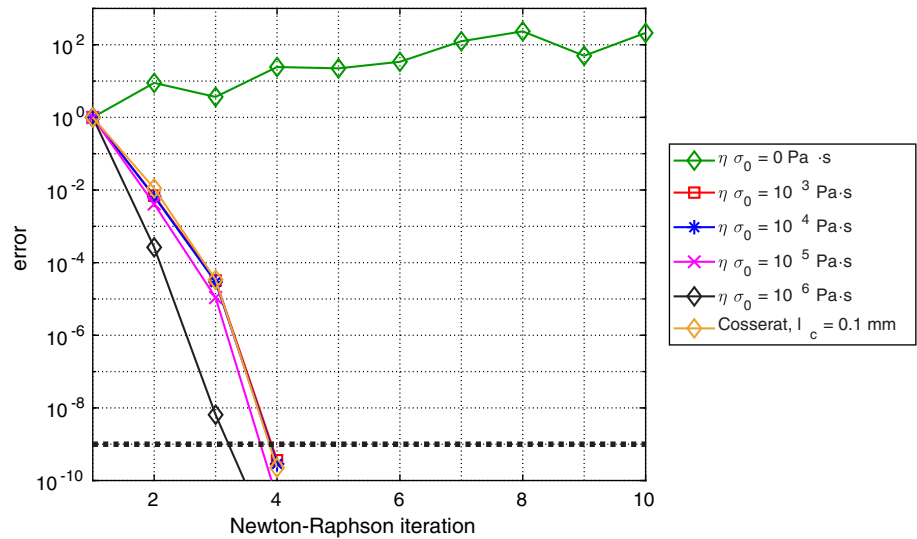
FIGURE 5 Convergence behavior for a standard continuum with and without viscoplasticity, and using a Cosserat continuum without viscoplasticity for $t_t = 0.2$ MPa, $\Delta t = 0.1$ ms [Color figure can be viewed at wileyonlinelibrary.com]
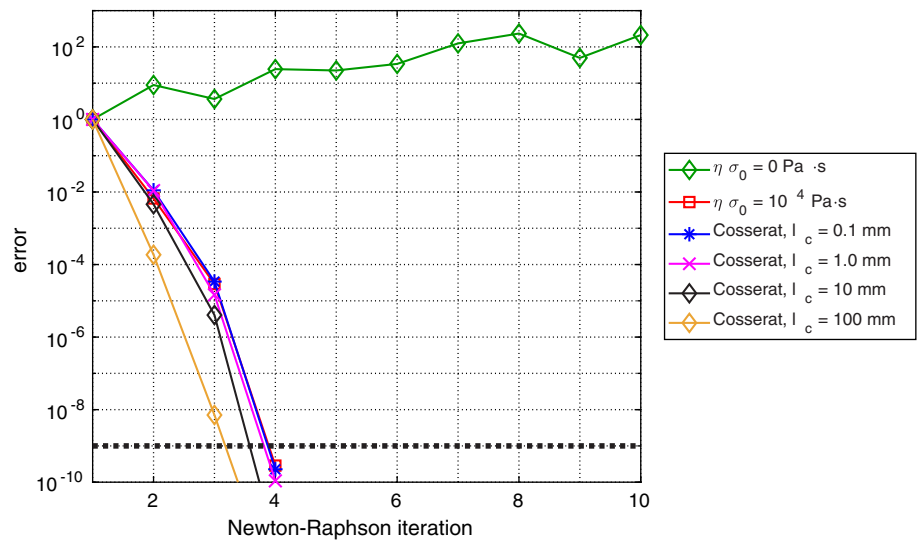
continuum is approximately four to five times the internal length scale ℓ_c,[21] the distance over which a sharp interface is smoothened, is comparable for $\ell_c = 0.1$ mm and $\ell_v = 0.4$ mm, and so on.

The domain was discretized using cubic T-splines. Near the fracture 40 Bézier extracted elements were used in the horizontal direction, while just 10 large elements were used away from the fracture, as shown in Figure 2(B). Twenty elements were used in the vertical direction (six small, six medium, and eight large elements). The refinement near the interface was chosen to accurately capture the stress and plasticity near the fracture tip, while using the increased accuracy of T-splines to allow for larger elements away from the centre. The Newmark time discretization scheme was used with $\beta = 0.4$ and $\gamma = 0.75$. The Newton-Raphson scheme was considered as converged when error$<10^{-9}$.

The convergence during the first step in which plasticity occurs, is shown in Figure 4 for the case with $t_t = 0.2$ MPa. The simulation which uses a standard continuum without viscoplasticity does not converge. Adding viscosity reduces the oscillations, and results in a quadratic convergence rate for all simulations. This convergence is fairly independent of the value of the viscosity parameter. Only for very large values the convergence further improves, for example, for $\eta\sigma_0 = 10^6$ Pa · s.

The results for a Cosserat continuum exhibit quadratic convergence without adding viscosity, as shown in Figure 5. The quadratic convergence is independent of the value of the internal length scale and an increase of the internal length scale only slightly improves the convergence.

The results for a twice as high shear stress and a time step which is 10 times as big, are shown in Figure 6. Similar to the first case, the use of viscosity or a Cosserat continuum result in a quadratic rate of convergence, independent of the value
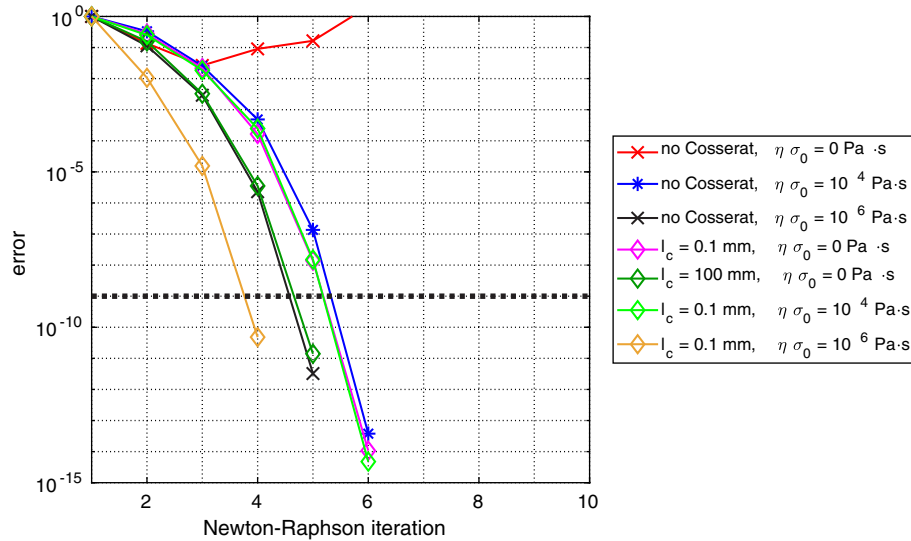
FIGURE 6 Convergence behavior for a standard continuum, and for a Cosserat continuum for $t_t = 0.4$ MPa, $\Delta t = 1$ ms [Color figure can be viewed at wileyonlinelibrary.com]
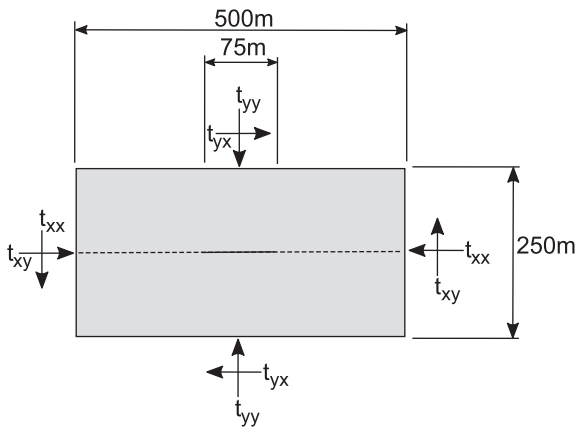
FIGURE 7 Geometry used for the combination of fracture propagation and non-associated plasticity

of the internal length scale. Adding a small amount of viscoplasticity in the Cosserat continuum does not significantly alter the convergence behavior, but using a large value for the viscosity results in an improved convergence, just like when using a large value for the internal length scale in the Cosserat continuum.

The results show that both the Cosserat continuum and viscoplasticity regularize the ill-posed character of the boundary value problem introduced by the use of a non-associated flow rule in plasticity. Comparing the convergence between the standard continuum with viscoplasticity and the Cosserat continuum shows that both these methods obtain similar convergence rates, and that an increase in the internal length scale does not significantly alter the convergence as long as the problem is not dominated by it.

5 | FRACTURE PROPAGATION

To show the ability of a Cosserat continuum to simulate fracture propagation in combination with off-fault, non-associated plasticity, a typical fracture propagation/plasticity problem has been simulated.[8] A rectangular domain is considered of 500 m $\times$ 250 m with a 75 m fracture at the center, shown in Figure 7. Absorbing boundary conditions are applied, and tractions $t_{xx} = 8.55$ MPa, $t_{yy} = 10$ MPa, $t_{xy} = t_{yx} = 1.8$ MPa have been imposed. Simulations have been carried out using a Cosserat continuum without viscoplasticity, and a standard continuum using viscoplasticity with $\eta\sigma_0 = 10^5$ Pa $\cdot$ s ($\ell_v = 40$ mm). Drucker-Prager plasticity has been used with a cohesion $c = 0$, $\phi = 31°$, and $\psi = 0°$. A Cosserat length scale $\ell_c = 10$ mm has been used. All other properties are identical to those in Section 4.

A mesh of (160/80/40) $\times$ 40 Bézier elements has been used in Section 5.1. Similar to the previous case, coarser elements are used away from the interface: 160 small elements in a horizontal sense close to the interface, 80 elements in
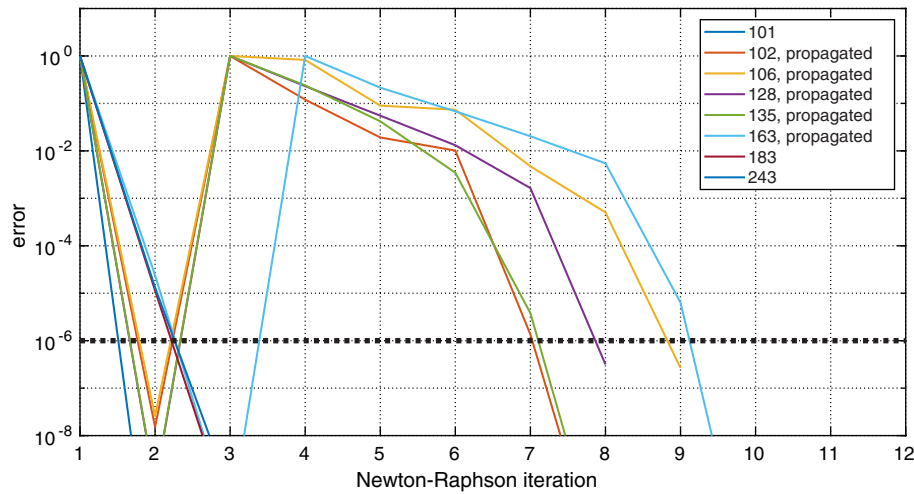
FIGURE 8
Deformations at $t = 1.15$ s
[Color figure can be viewed at wileyonlinelibrary.com]
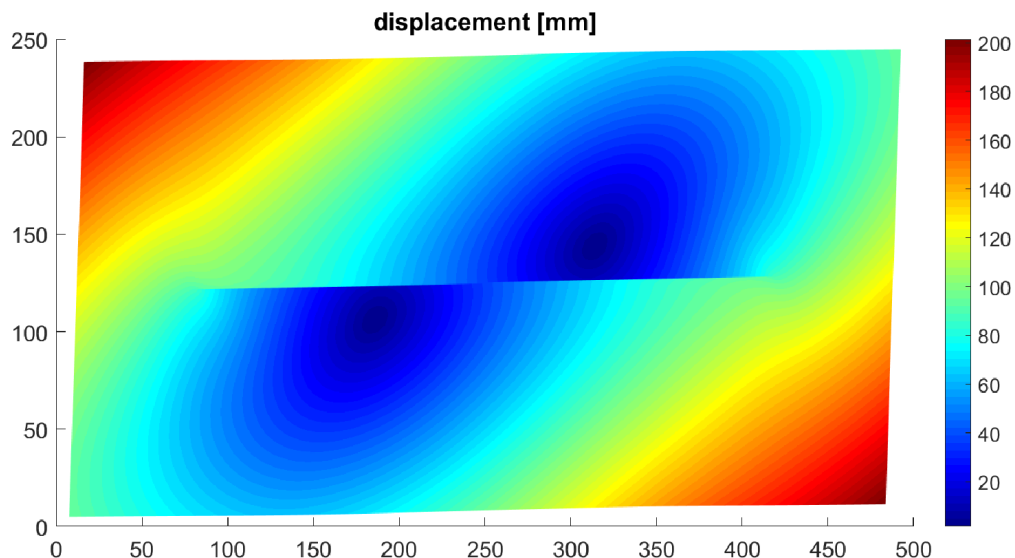
FIGURE 9   Cosserat rotation at $t = 1.15$ s [Color figure can be viewed at wileyonlinelibrary.com]
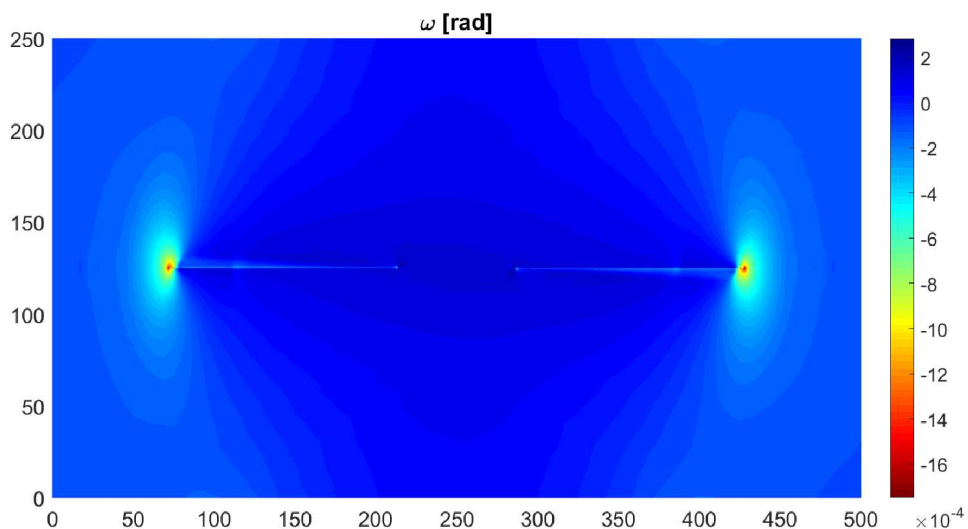

a horizontal sense as medium sized elements, and 40 large elements away from the interface. To investigate the effect of the element size, two more meshes are used in Section 5.2: A mesh using $(320/160/80) \times 50$ elements with similar coarsening as the first mesh, and a mesh with an extra refinement layer near the interface resulting in $(640/320/160/80) \times 56$ elements. The vertical element size was chosen such that all but the largest elements were square.

In Section 5.1 a time step size $\Delta t = 1$ ms is used. This step size corresponds to the fracture propagating approximately every other time step. This is in contrast to explicit time integration schemes, which require several time steps per discrete fracture propagation.[9] In Section 5.2 a smaller time step will be used to eliminate the time step size as a possible source of errors, with the time step size chosen such that approximately 10 time steps are needed for a pressure wave to pass through the smallest element: $\Delta t = 0.2$ ms for the coarse mesh, $\Delta t = 0.1$ ms for the medium mesh, and $\Delta t = 0.04$ ms for the finest mesh. All simulations first use a time step of $\Delta t = 10$ ms to reach an initial equilibrium condition at $t = 1$ s, after which plasticity and fracture propagation is allowed, and the smaller time step sizes are used.

The fracture is allowed to propagate along the predefined horizontal path, reaching the end of the domain after approximately 0.25 s. The computed displacements are shown in Figure 8. Figure 9 shows the Cosserat micro-rotation being close to zero in most of the domain. The rotation is highest near the fracture tip, which is the location where most plasticity occurs and therefore requires a strong regularizing effect. Since the Cosserat rotation is close to zero at the domain boundaries, the assumption is validated that the Cosserat rotation does not need to be prescribed in the absorbing boundary conditions.

FIGURE 10 Convergence during selected time steps without Cosserat continuum ($\eta\sigma_0 = 10^5$ Pa · s) using the 160×40 mesh with $\Delta t = 1.0$ ms [Color figure can be viewed at wileyonlinelibrary.com]
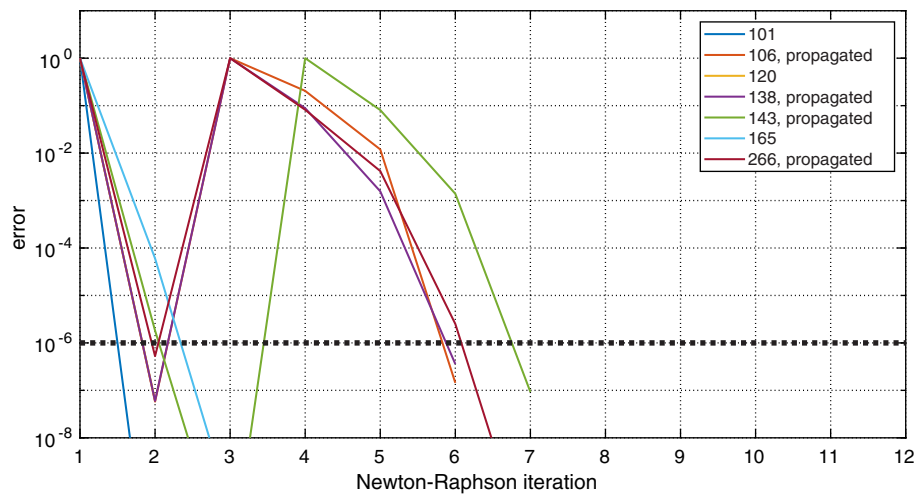
FIGURE 11 Convergence during selected time-steps using a Cosserat continuum ($\ell_c = 10$ mm) using the 160×40 mesh with $\Delta t = 1.0$ ms [Color figure can be viewed at wileyonlinelibrary.com]

5.1 | Convergence behavior

An example of the convergence behavior using a standard continuum equipped with viscoplasticity is shown in Figure 10. The peaks in the error are a result of the fracture propagating once convergence has been reached, thereby requiring the error associated with the propagated fracture to be reduced again. Time steps in which no fracture propagation occurs, converge in two to three iterations, and time steps with fracture propagation show a quadratic convergence rate after the fracture has propagated (although with some oscillations during the first few iterations).

Figure 11 shows the convergence using a Cosserat continuum. No viscoplasticity was included as regularization in this simulation. Similar to the standard continuum with viscoplasticity, the steps in which no fracture propagation is observed, show quadratic convergence, and converge within two to three iterations. When the fracture propagates, quadratic convergence can be observed starting from the new position. As for viscoplasticity, all steps converge within 10 iterations, also when the fracture propagates, but oscillations are now not observed.

These results confirm the results from Section 4 that a Cosserat continuum properly regularizes the ill-posedness introduced by non-associated plasticity, and as a consequence, results in vastly improved convergence characteristics compared to a standard continuum. Indeed, quadratic convergence is obtained even in the presence of abrupt changes in the stress field due to fracture propagation. A standard continuum, however, requires the inclusion of viscoplasticity to regularize the ill-posedness. For both cases, an implicit time discretization scheme can use large time steps without becoming unstable and without convergence issues. The simulation with the 160×40 mesh only requires 350 time steps (including 100 to apply the initial conditions) which corresponds to a new interface element fracturing every few steps. This is very different from most explicit time integration schemes, which often require a number of time steps per discrete fracture propagation step.

FIGURE 12 Plastic strain after $t = 1.2$ s around the right fracture tip using a Cosserat continuum ($\ell_c = 10$ mm). (A) 160×140 (three refinement layers); (B) 320×50 (three refinement layers); (C) 640×56 (four refinement layers) [Color figure can be viewed at wileyonlinelibrary.com]

(A) 160×40 (3 refinement layers)

(B) 320×50 (3 refinement layers)

(C) 640×56 (4 refinement layers)
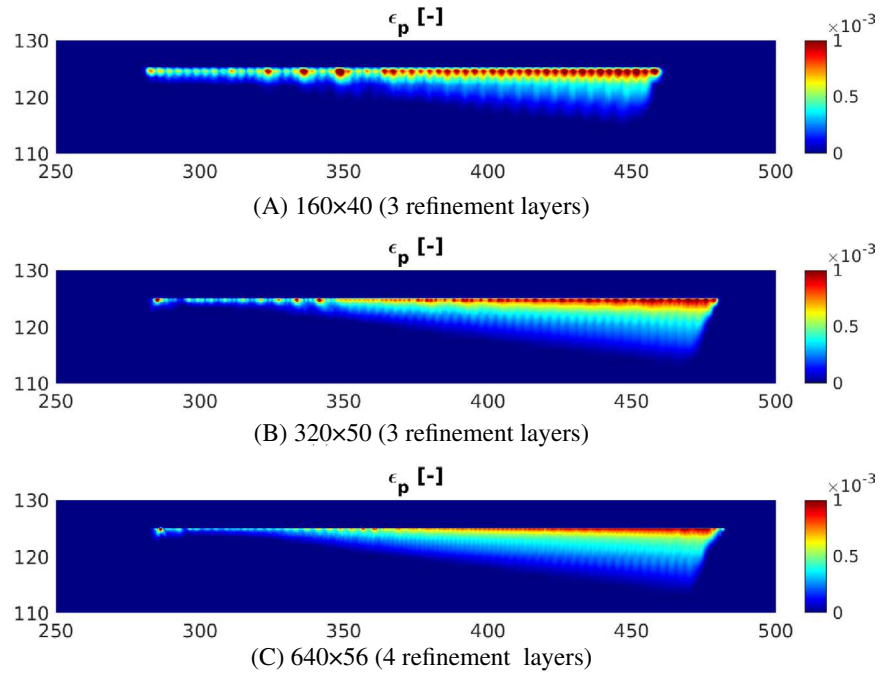
5.2 │ Element size dependence

Simulations using three meshes have been carried out to analyze the influence of the element size in a Cosserat continuum with interface elements. For comparison, simulations have also been carried out using a standard continuum with viscoplasticity, using the viscosity parameter from the previous section ($\eta \sigma_0 = 10^5$ Pa · s).

The results for the Cosserat continuum are shown in Figure 12. The plastic strain for the coarsest mesh shows a clear effect of the interface elements. Due to the element-wise fracture propagation, stress concentrations occur near the fracture tips, whereas lower stresses occur in the center of the interface elements. This results in more plastic strain near the beginning and the end of the interface elements, while less plastic strain occurs in the centre of the interface elements. When the mesh is refined, the influence of the interface element size becomes smaller. The results using the 320×50 mesh still show a slight increase in plastic strain corresponding to the element size, but further refining the mesh reduces this effect.

For the plastic strain away from the interface the effect of the interface element size becomes smaller. While the coarsest mesh still shows a clear influence of the element size near the interface, the plastic strain is smoothened in the interior. The other two meshes show similar results, with near to no difference in the plastic strains in the interior.

The same element size dependence is also seen when a standard continuum with viscoplastic regularization is used, as shown in Figure 13. Similar to the Cosserat continuum, peaks in the plastic strain are observed near the fracture, and these peaks reduce upon mesh refinement. The effect of the "plasticity peaks" can also be seen in the shear stress near the discontinuity, Figure 14. The uneven plastic strains result in oscillations in the shear stress along the fracture for the coarsest mesh. Similar to the results for the plastic strains, the finer meshes show smaller oscillations, with the finest mesh only showing a peak in the shear stress at the location of the original fracture tip.

Considering the fracture length, shown in Figure 15, the influence of the element size is also observed. Due to the element-wise fracture propagation, steps in the fracture length occur for all meshes, with the steps most notable for the coarsest mesh. While the coarsest mesh shows a difference in fracture length compared to the two other meshes, all three meshes result in a fracture propagation velocity of approximately 80% of the shear wave velocity. Furthermore, while small differences in plastic strain are observed between the finer meshes, these differences do not appear to significantly influence the stress, and therefore the fracture propagation.

5.3 │ Influence of the internal length scale

In Section 4 it has been shown that increasing the internal length scale, either the Cosserat length scale or the viscosity parameter, results in an improved convergence. However, when the original problem does not include viscoplasticity

(A) 160×40 (3 refinement layers)

(B) 320×50 (3 refinement layers)

(C) 640×56 (4 refinement layers)
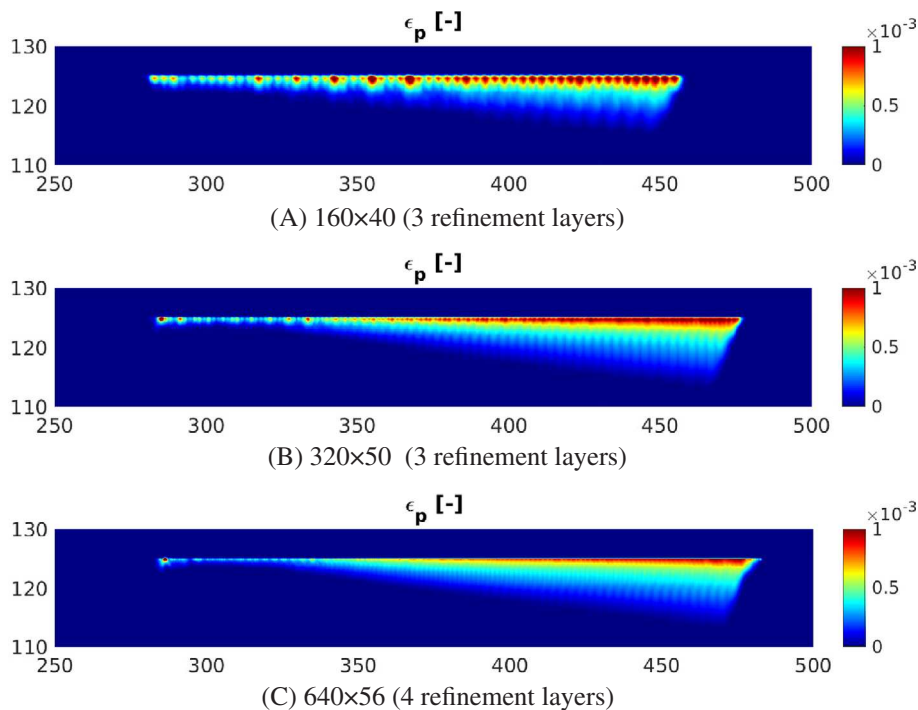
FIGURE 13 Plastic strain after $t = 1.2$ s around the right fracture tip using a standard continuum with $\eta\sigma_0 = 10^5$ Pa $\cdot$ s. (A) 160×40 (three refinement layers); (B) 320×50 (three refinement layers); (C) 640×56 (four refinement layers) [Color figure can be viewed at wileyonlinelibrary.com]

(A) 160×40 (3 refinement layers)

(B) 320×50 (3 refinement layers)

(C) 640×56 (4 refinement layers)
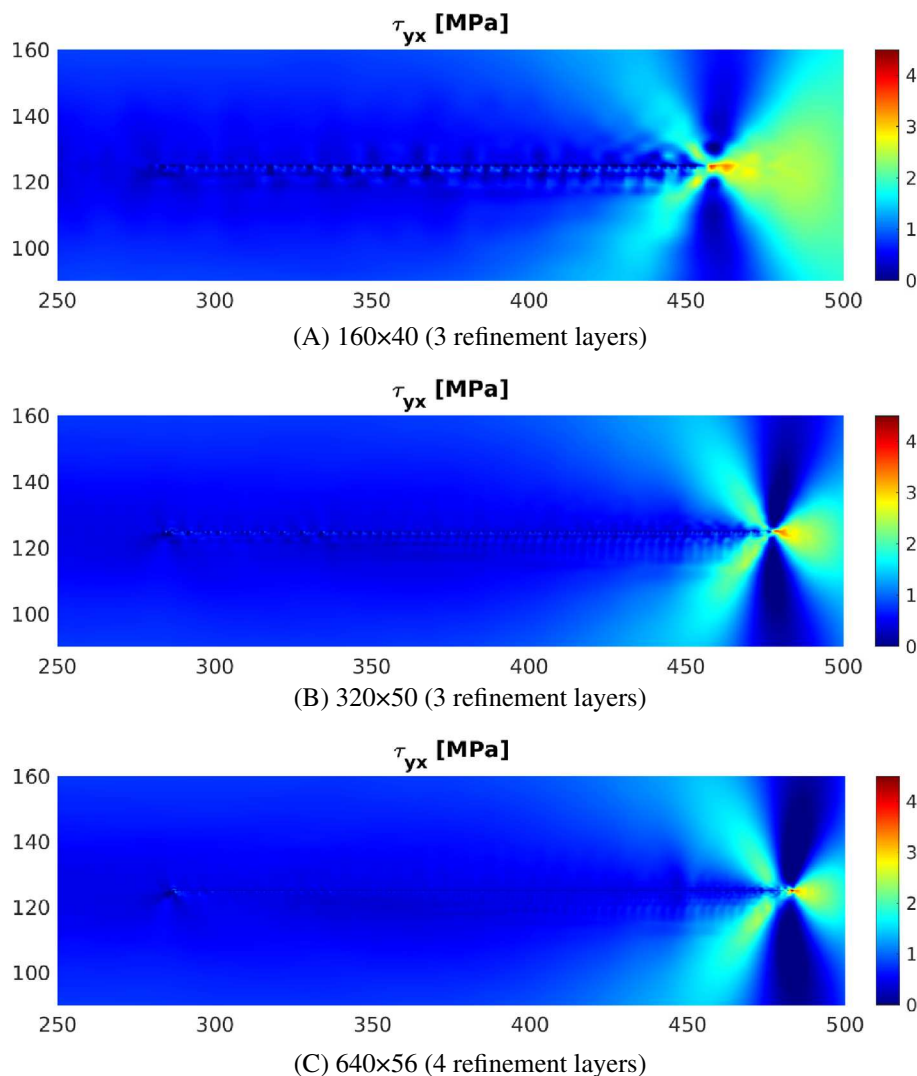
FIGURE 14 Shear stress at $t = 1.2$ s around the right fracture using a Cosserat continuum. (A) 160×40 (three refinement layers); (B) 320×50 (three refinement layers); (C) 640×56 (four refinement layers) [Color figure can be viewed at wileyonlinelibrary.com]

FIGURE 15 Fracture length using the 160×40, 320×50, and 640×56 meshes using the standard and Cosserat continua [Color figure can be viewed at wileyonlinelibrary.com]

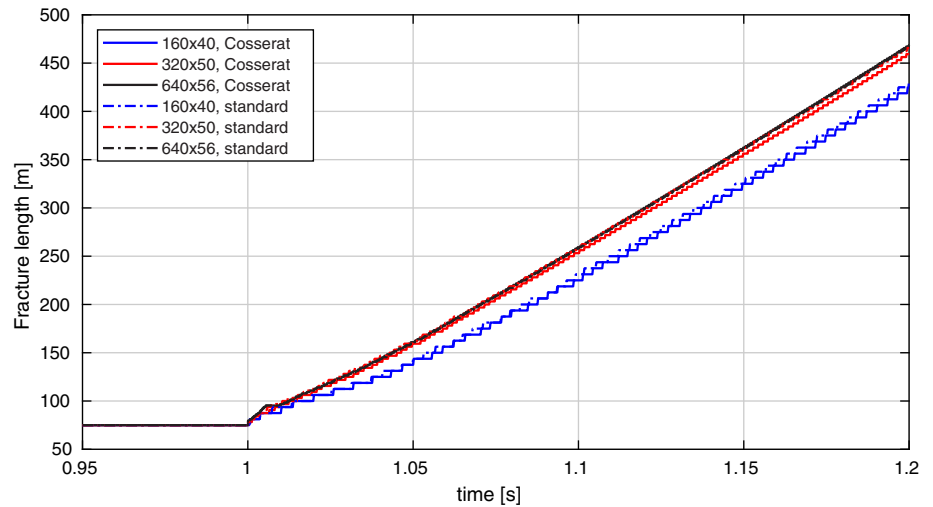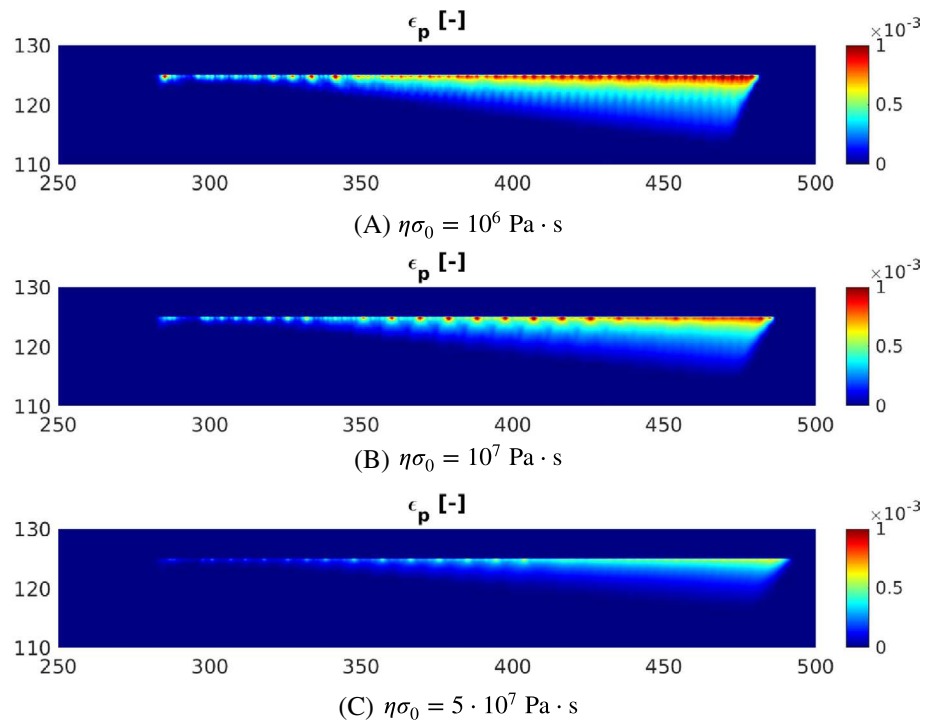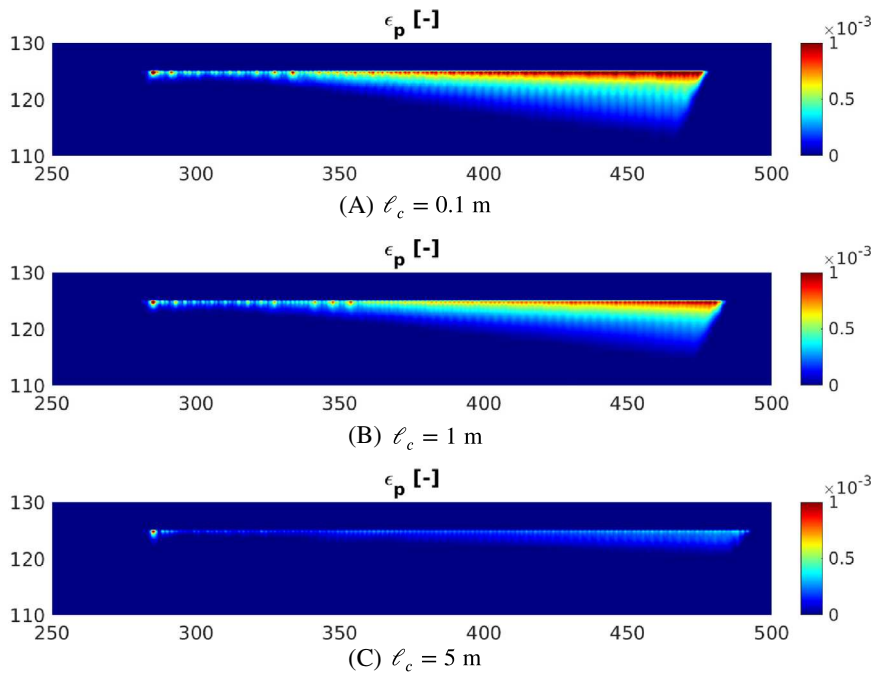

FIGURE 16 Plastic strain after $t = 1.2$ s around the right fracture tip using a standard continuum with the 320×50 mesh. (A) $\eta\sigma_0 = 10^6$ Pa· s; (B) $\eta\sigma_0 = 10^7$ Pa· s; (C)$\eta\sigma_0 = 5 \cdot 10^7$ Pa· s [Color figure can be viewed at wileyonlinelibrary.com]

(A) $\eta\sigma_0 = 10^6$ Pa · s

(B) $\eta\sigma_0 = 10^7$ Pa · s

(C) $\eta\sigma_0 = 5 \cdot 10^7$ Pa · s

an increase of the viscosity parameter may more and more depart from the original problem. This is demonstrated in Figure 16 through simulations (320×50 mesh) for high values of the viscosity: $\eta\sigma_0 = 10^6$ Pa · s, $\eta\sigma_0 = 10^7$ Pa · s and $\eta\sigma_0 = 5 \cdot 10^7$ Pa · s. Increasing the viscosity reduces the "plasticity peaks," but also limits the plastic strain that is obtained. Furthermore, since the viscoplasticity model allows stresses to exceed the yield surface, higher stresses are present near the fracture tip, resulting in a slightly faster fracture propagation.

Simulations using larger Cosserat length scales, Figure 17, show that increasing the Cosserat length scale does not alter the fracture propagation as much as adding viscosity, until the Cosserat length scale becomes similar to the size of the plastically deformed zone. While the simulations with the viscoplastic continuum preserve the triangular shape of the zone in which plastic deformations occur, increasing the Cosserat length scale rounds this zone near the fracture tip. An increase of the Cosserat length scale also smoothens the stresses, resulting in smaller plastic strains near the discontinuity. The results for a large Cosserat length scale show that this length scale suppresses the plastic deformations more compared to using a high amount of viscoplasticity. This is the opposite of the behavior for lower length scales, where the Cosserat continuum allows for more plastic straining.

FIGURE 17 Plastic strain after $t = 1.2$ s around the right fracture tip using a Cosserat continuum with the 320×50 mesh. (A)$\ell_c = 0.1$ m (B)$\ell_c = 1$ m (C)$\ell_c = 5$ m [Color figure can be viewed at wileyonlinelibrary.com]

6 | CONCLUDING REMARKS

A Cosserat continuum as well as a standard continuum, each with and without viscosity, have been used to simulate the combined problem of fracture propagation and non-associated, off-fault plasticity. Since non-associated plasticity can render the boundary value problem ill-posed for low positive or zero hardening rates, enrichment using a Cosserat continuum or a viscoplastic regularization is necessary to retrieve a well-posed problem. For the first time, the efficacy of these two regularization strategies has been compared and quantified for non-associated plasticity, using a range of values for the internal length scale. In particular, the effects on the convergence of the nonlinear solution strategy, in this case Newton-Raphson, has been investigated. Moreover, the effects of two dissipative mechanisms—fracture and plasticity—acting simultaneously, have been assessed.

The first series of simulations employ a stationary crack. The simulations with a standard continuum show issues with convergence, which could only be resolved by adding viscosity and/or using a Cosserat continuum. Then, a quadratic convergence for a Newton-Raphson solver results, indicating that for both enrichments a well-posed initial value problem is obtained. An increase of the Cosserat length scale or viscosity parameter improves the convergence, but very large values may alter the physics and result in solutions with limited plastic deformations. More complex simulations which include a propagating fracture lead to the same conclusions.

Finally, simulations have been carried out to investigate the effect of the element size in the presence of fractures. They show that in the interior of the domain a coarse mesh is sufficient to accurately represent the deformations, stresses, and plastic strains. However, closer to the fracture small elements are needed to smoothen the plastic strain fields. Else, "plastic strain peaks" can be observed which are caused by the element-wise fracture propagation, and are therefore removed only when using smaller elements at the interface. Increasing the value of the internal length scale shows that, while the convergence is further improved, and "plasticity peaks" are reduced, it may at some point start to alter the physics of the problem, resulting in smaller plastic strains and changes in the region in which plastic deformations occur.

ORCID
Tim Hageman https://orcid.org/0000-0001-7770-7440
Sepideh Alizadeh Sabet https://orcid.org/0000-0002-5316-8152
René de Borst https://orcid.org/0000-0002-3457-3574

REFERENCES

1. Vermeer PA, de Borst R. Non-associated plasticity for soils concrete and rock. *Heron*. 1984;29(3):3-64.
2. de Borst R, Crisfield MA, Remmers JJC, Verhoosel CV. *Nonlinear Finite Element Analysis of Solids and Structures*. 2nd ed. Chichester: John Wiley & Sons; 2012.
3. Spiegelman M, May DA, Wilson CR. On the solvability of incompressible Stokes with viscoplastic rheologies in geodynamics. *Geochem Geophys Geosyst*. 2016;17:2213-2238.
4. Fraters MRT, Bangerth W, Thieulot C, Glerum A, Spakman W. Efficient and practical Newton solvers for non-linear Stokes systems in geodynamic problems. *Geophys J Int*. 2019;218:873-894.
5. Sabet SA, de Borst R. Structural softening, mesh dependence, and regularisation in non-associated plastic flow. *Int J Numer Anal Methods Geomech*. 2019;43:2170-2183.
6. Rudnicki JW, Rice JR. Conditions for the localization of deformation in pressure-sensitive dilatant materials. *J Mech Phys Solids*. 1975;23:371-394.
7. Sabet SA, de Borst R. Mesh bias and shear band inclination in standard and non-standard continua. *Arch Appl Mech*. 2019;89:2577-2590.
8. Templeton EL, Rice JR. Off-fault plasticity and earthquake rupture dynamics: 1. dry materials or neglect of fluid pressure changes. *J Geophys Res*. 2008;113(B9):B09306.
9. Viesca RC, Templeton EL, Rice JR. Off-fault plasticity and earthquake rupture dynamics: 2. effects of fluid saturation. *J Geophys Res*. 2008;113(B9):B09307.
10. Erickson BA, Dunham EM, Khosravifar A. A finite difference method for off-fault plasticity throughout the earthquake cycle. *J Mech Phys Solids*. 2017;109:50-77.
11. Dunham EM, Belanger D, Cong L, Kozdon JE. Earthquake ruptures with strongly rate-weakening friction and off-fault plasticity, Part 1: planar faults. *Bull Seismol Soc Am*. 2011;101:2296-2307.
12. de Borst R, Sluys LJ, Muhlhaus HB, Pamin J. Fundamental issues in finite element analyses of localization of deformation. *Eng Comput*. 1993;10:99-121.
13. Mühlhaus HB, Vardoulakis I. The thickness of shear bands in granular materials. *Géotechnique*. 1987;37:271-283.
14. Cosserat E, Cosserat F. *Théorie des Corps Deformables*. Paris: A. Hermann et fils; 1909.
15. Khoei AR, Tabarraie AR, Gharehbaghi SA. H-adaptive mesh refinement for shear band localization in elasto-plasticity Cosserat continuum. *Commun Nonlinear Sci Numer Simul*. 2005;10:253-286.
16. Ebrahimian B, Noorzad A, Alsaleh MI. Modeling shear localization along granular soil-structure interfaces using elasto-plastic Cosserat continuum. *Int J Solids Struct*. 2012;49:257-278.
17. Khoei AR, Karimi K. An enriched-FEM model for simulation of localization phenomenon in Cosserat continuum theory. *Comput Mater Sci*. 2008;44:733-749.
18. Manzari MT. Application of micropolar plasticity to post failure analysis in geomechanics. *Int J Numer Anal Methods Geomech*. 2004;28:1011-1032.
19. Adhikary DP, Dyskin AV. A continuum model of layered rock masses with non-associative joint plasticity. *Int J Numer Anal Methods Geomech*. 1998;22:245-261.
20. Veveakis E, Sulem J, Stefanou I. Modeling of fault gouges with Cosserat continuum mechanics: Influence of thermal pressurization and chemical decomposition as coseismic weakening mechanisms. *J Struct Geol*. 2012;38:254-264.
21. de Borst R, Sluys LJ. Localisation in a Cosserat continuum under static and dynamic loading conditions. *Comput Methods Appl Mech Eng*. 1991;90:805-827.
22. de Borst R. Simulation of strain localization: a reappraisal of the Cosserat continuum. *Eng Comput*. 1991;8:317-332.
23. Neff P, Chelminski K. Well-posedness of dynamic Cosserat plasticity. *Appl Math Optim*. 2007;56:19-35.
24. Needleman A. Material rate dependence and mesh sensitivity in localization problems. *Comput Methods Appl Mech Eng*. 1988;67:69-85.
25. Sluys LJ, de Borst R. Wave propagation and localization in a rate-dependent cracked medium – model formulation and one-dimensional examples. *Int J Solids Struct*. 1992;29:2945-2958.
26. Wang WM, Sluys LJ, de Borst R. Viscoplasticity for instabilities due to strain softening and strain-rate softening. *Int J Numer Methods Eng*. 1997;40:3839-3864.
27. Duretz T, de Borst R, Le Pourhiet L. Finite thickness of shear bands in frictional viscoplasticity and implications for lithosphere dynamics. *Geochem Geophys Geosyst*. 2019;20:5590-5616.
28. de Borst R, Duretz T. On viscoplastic regularisation of strain-softening rocks and soils. *Int J Numer Anal Methods Geomech*. 2020;44:890-903.
29. Schellekens JCJ, de Borst R. The application of interface elements and enriched or rate-dependent continua to micro-mechanical analyses of fracture in composites. *Comput Mech*. 1994;14:68-83.
30. Cormeau I. Numerical stability in quasi-static elasto/visco-plasticity. *Int J Numer Methods Eng*. 1975;9:109-127.
31. Cervera M, Chiumenti M, Agelet de Saracibar C. Softening, localization and stabilization: capture of discontinuous solutions in J2 plasticity. *Int J Numer Anal Methods Geomech*. 2004;28:373-393.
32. Bazilevs Y, Calo VM, Cottrell JA, et al. Isogeometric analysis using T-splines. *Comput Methods Appl Mech Eng*. 2010;199:229-263.
33. Hughes TJR, Cottrell JA, Bazilevs Y. Isogeometric analysis: CAD, finite elements, NURBS exact geometry and mesh refinement. *Comput Methods Appl Mech Eng*. 2005;194:4135-4195.
34. May S, Vignollet J, de Borst R. The role of the Bézier extraction operator for T-splines of arbitrary degree: linear dependencies, partition of unity property nesting behaviour and local refinement. *Int J Numer Methods Eng*. 2015;103:547-581.

35. Chen L, de Borst R. Locally refined T-splines. *Int J Numer Methods Eng*. 2018;114:637-659.

36. Scott MA, Li X, Sederberg TW, Hughes TJR. Local refinement of analysis-suitable T-splines. *Comput Methods Appl Mech Eng*. 2012;213-216:206-222.

37. Chen L, Verhoosel CV, de Borst R. Discrete fracture analysis using locally refined T-splines. *Int J Numer Methods Eng*. 2018;116:117-140.

38. Elguedj T, Hughes TJR. Isogeometric analysis of nearly incompressible large strain plasticity. *Comput Methods Appl Mech Eng*. 2014;268:388-416.

39. Kolo I, de Borst R. An isogeometric analysis approach to gradient-dependent plasticity. *Int J Numer Methods Eng*. 2018;113:296-310.

40. Yu T, Lai W, Bui TQ. Three-dimensional elastoplastic solids simulation by an effective IGA based on Bézier extraction of NURBS. *Int J Mech Mater Des*. 2019;15:175-197.

41. de Borst R. A generalisation of J2-flow theory for polar continua. *Comput Methods Appl Mech Eng*. 1993;103:347-362.

42. Kame N, Rice JR, Dmowska R. Effects of prestress state and rupture velocity on dynamic fault branching. *J Geophys Res Solid Earth*. 2003;108(B5):2265.

43. Scott MA, Borden MJ, Verhoosel CV, Sederberg TW, Hughes TJR. Isogeometric finite element data structures based on Bézier extraction of T-splines. *Int J Numer Methods Eng*. 2011;88:126-156.

44. Hageman T, de Borst R. Flow of non-Newtonian fluids in fractured porous media: isogeometric vs standard finite element discretizatio. *Int J Numer Anal Methods Geomech*. 2019;43:2020-2037.

45. Borden MJ, Scott MA, Evans JA, Hughes TJR. Isogeometric finite element data structures based on Bézier extraction of NURBS. *Int J Numer Methods Eng*. 2011;87:15-47.

46. Chen L, Li B, de Borst R. Energy conservation during remeshing in the analysis of dynamic fracture. *Int J Numer Methods Eng*. 2019;120:433-446.

47. Lysmer J, Kuhlemeyer RL. Finite dynamic model for infinite media. *ASCE J Eng Mech Div*. 1969;95:859-878.

48. Shih JY, Thompson DJ, Zervos A. The effect of boundary conditions, model size and damping models in the finite element modelling of a moving load on a track/ground system. *Soil Dyn Earthq Eng*. 2016;89:12-27.

49. Jin L, Zoback MD. Fully dynamic spontaneous rupture due to quasi-static pore pressure and poroelastic effects: an implicit nonlinear computational model of fluid-induced seismic events. *J Geophys Res Solid Earth*. 2018;123:9430-9468.

APPENDIX . INTERNAL FORCE VECTOR AND TANGENTIAL STIFFNESS MATRICES

The governing equations have been discretized using a finite element method, combined with Bézier extracted T-splines. The external force vector is defined in a standard manner as:

$$\boldsymbol{f}_{\text{ext}} = \int_{\Gamma} \boldsymbol{N}^T \boldsymbol{t} \, \mathrm{d}\Gamma, \tag{A1}$$

with $\boldsymbol{t}$ the traction imposed on the boundary Γ (the effects of the absorbing boundary are included in the internal forces). The internal forces are defined as:

$$\boldsymbol{f}_{int}^{t+\Delta t} = \int_{\Omega} \boldsymbol{B}^T \boldsymbol{\sigma}_{t+\Delta t} + \boldsymbol{N}^T \rho \boldsymbol{N} \ddot{\boldsymbol{u}}_{t+\Delta t} \, \mathrm{d}\Omega + \int_{\Gamma_d} \boldsymbol{N}_i^T \boldsymbol{R}^T \boldsymbol{D}_i \boldsymbol{R} \boldsymbol{N}_i \boldsymbol{u}_{t+\Delta t} + \boldsymbol{N}_i^T \boldsymbol{R}^T (\boldsymbol{\tau}_{czm})_{t+\Delta t} \, \mathrm{d}\Gamma_d + \int_{\Gamma} \boldsymbol{N}^T \boldsymbol{R}^T \boldsymbol{C} \boldsymbol{R} \boldsymbol{N} \dot{\boldsymbol{u}}_{t+\Delta t} \, \mathrm{d}\Gamma, \tag{A2}$$

with $\boldsymbol{R}$ the rotation matrix for the interface and boundary elements, $\boldsymbol{\tau}_{czm}$ the tractions in tangential direction resulting from Equation (12), and the dummy stiffness matrix and interface jump matrix defined as:

$$\boldsymbol{D}_i = \begin{bmatrix} d_n & 0 & 0 \\ 0 & 0 & 0 \\ 0 & 0 & d_\omega \end{bmatrix} \quad \boldsymbol{N}_i = \begin{bmatrix} -\boldsymbol{N}_x & \boldsymbol{N}_x & 0 & 0 & 0 & 0 \\ 0 & 0 & -\boldsymbol{N}_y & \boldsymbol{N}_y & 0 & 0 \\ 0 & 0 & 0 & 0 & -\ell_c \boldsymbol{N}_\omega & \ell_c \boldsymbol{N}_\omega \end{bmatrix}.$$

The interface jump matrix is defined such that the jump is given in local coordinates by $[\![u_n \; u_t \; \ell_c\omega]^T]\!] = \boldsymbol{RN_i u}$. Since interface elements are only inserted for fractured elements, the dummy stiffness matrix contains terms to enforce a continuous Cosserat rotation and to prevent negative opening heights, while the tangential traction is included through the slip model. The term which contains the interface dummy stiffness $\boldsymbol{D}_i$ is integrated using lumped integration, whereas all other terms are integrated using a Gauss integration scheme. This lumped integration prevents traction oscillations on the interface as a result of the dummy stiffness.

The tangential stiffness matrix required for the iterative Newton-Raphson algorithm reads:

$$\left(\frac{\partial \boldsymbol{f}_{\text{int}}}{\partial \boldsymbol{u}}\right)_{t+\Delta t} = \int_{\Omega} \boldsymbol{B}^T \boldsymbol{D}_{\text{eff}} \boldsymbol{B} + \frac{1}{\beta \Delta t^2} \boldsymbol{N}^T \rho \boldsymbol{N} \, d\Omega + \int_{\Gamma_d} \boldsymbol{N}_i^T \boldsymbol{R}^T \boldsymbol{D}_i \boldsymbol{R} \boldsymbol{N}_i + \boldsymbol{N}_i^T \boldsymbol{R}^T \boldsymbol{D}_{\text{czm}} \boldsymbol{R} \boldsymbol{N}_i \, d\Gamma_d + \int_{\Gamma} \frac{\gamma}{\beta \Delta t} \boldsymbol{N}^T \boldsymbol{R}^T \boldsymbol{C} \boldsymbol{R} \boldsymbol{N} \, d\Gamma, \quad (A3)$$

with $\boldsymbol{D}_{\text{eff}}$ depending on the plastic strain increment through $\widehat{\Delta\lambda}$. The matrix $\boldsymbol{D}_{\text{czm}}$ depends on whether the tangential displacement at the interface is higher than the maximum tangential displacement saved as history variable $[\![dx]\!]$. If the history variable is higher, the nonzero component of $\boldsymbol{D}_{\text{czm}}$ is given by:

$$\boldsymbol{D}_{\text{czm}}(t, n) = -f_r d_n + (f_p - f_r) \exp(-2 [\![dx]\!] / D_c)(-d_n + d_n [\![u_n]\!] \cdot 2 [\![dx]\!] / D_c^2 \cdot 2\mathcal{G}_c / ((f_p - f_r)d_n [\![u_n]\!]^2)),$$

whereas if the current tangential displacement is higher, the nonzero components are:

$$\boldsymbol{D}_{\text{czm}}(t, t) = 2(f_p - f_r)d_n [\![u_n]\!] / D_c \exp(-2 [\![u_t]\!] / D_c)$$

$$\boldsymbol{D}_{\text{czm}}(t, n) = -f_r d_n + (f_p - f_r) \exp(-2 [\![u_t]\!] / D_c)(-d_n + d_n [\![u_n]\!] \cdot 2 [\![u_t]\!] / D_c^2 \cdot 2\mathcal{G}_c / ((f_p - f_r)d_n [\![u_n]\!]^2)),$$

with $[\![u_n]\!]$ and $[\![u_t]\!]$ the displacement jump in the normal and tangential directions in the integration point at time $t + \Delta t$.